THE JOURNAL OF PHYSICAL CHEMISTRY B

Article

pubs.acs.org/JPCB

Anthrax Edema Factor: An Ion-Adaptive Mechanism of Catalysis with Increased Transition-State Conformational Flexibility

Gabriel E. Jara and Leandro Martínez*

Institute of Chemistry, University of Campinas, Campinas, SP 13083-861, Brazil

Supporting Information

ABSTRACT: Edema Factor (EF) is one of three major toxins of anthrax. EF is an adenylyl cyclase that disrupts cell signaling by accelerating the conversion of ATP into cyclic-AMP. EF has a much higher catalytic rate than that of mammalian adenylyl cyclases (mACs). Crystal structures were obtained for mACs and EF, but the molecular basis for different catalytic activities remained poorly understood. In particular, the arrangement of the active site in EF is unclear in what concerns the number of ions present and the conformation of the substrate. Here, we use quantum mechanics−molecular mechanics simulations to estimate the free-energy profiles for the reaction catalyzed by EF and a mAC. We found that EF catalysis is possible, and faster than that of mACs, in both one and two Mg^{2+}-ion-binding modes, providing adaptive plasticity to host-cell environments. In both enzymes, the reaction mechanisms are highly associative. However, mechanistic differences exist. In the mAC, the nucleophile oxygen (ATP-O3′) is consistently coordinated to one of the Mg^{2+} ions, increasing its acidity. In EF, on the other hand, this coordination is eventual and not essential for the reaction to proceed. The persistent coordination of O3′ to the ion is favored in mACs by a greater ion partial charge. In EF, the reduced acidity of the O3′ oxygen is compensated by the presence of the His351 residue for proton abstraction. As proton transfer in EF does not require persistent attachment of the substrate to an ion, the substrate (ATP) and transition state display greater conformational flexibilities. These greater flexibilities allow the sampling of lower-energy conformations and might represent an entropic advantage for catalytic efficiency.

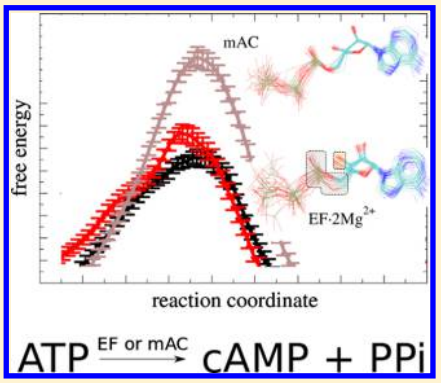

INTRODUCTION

The anthrax edema factor (EF) is one of the three major toxins secreted by *Bacillus anthracis*. It consists of an adenylyl cyclase (AC), converting ATP into cyclic-AMP (cAMP) (Figure 1). cAMP overproduction leads to the disruption of host cell signaling. EF is a Class II AC, and as such, it requires host cellular factors for activation, notably Calmodulin. Similar Class II ACs are found in whooping cough and plague bacteria, among other important pathogens.[1,2] EF has a catalytic rate at least 100-fold higher than that of mammalian adenylyl cyclases (mACs).[3,4] EF and mAC enzymes require Mg^{2+} ions in the catalytic site to be active. The arrangement of the active site of mACs was consistently determined from several crystal structures and supporting functional data and has been shown to depend on the binding of two metal ions to the active site (Figure 2D).[5] On the other hand, EF structures were obtained with different substrate conformations and active-site-ion-binding modes,[3,4,6] suggesting either crystallographic artifacts or some degree of promiscuity concerning the catalytic mechanism.[7] Therefore, the number of ions required for maximum efficiency in EF was not completely understood from the analysis of crystallographic models and is an important subject of debate.

Three crystal structures of the EF−Calmodulin complex were obtained (Figure 2A−C): two bound to ATP analogues (PDB id:1K90 and 1XFV) and the other bound to products (cAMP and pyrophosphate, PDB id: 1SK6).[3,4,6] The structures with the ATP mimic were obtained under different conditions: first, with a single ion in the active site (Figure 2A), although this ion was an Yb^{3+}.[3] Later, a product-bound structure (Figure 2C) was also obtained in the presence of Yb^{3+} and, interestingly, multiple ion occupancies were observed. Electron densities were observed in positions which could correspond to the presence of either one or two ions in the active site.[4] As mAC mechanisms, as well as the mechanisms of DNA polymerase and some endonucleases,[5,8] were recognized to depend on two catalytic ions (Figure 2D), an effort was made to obtain an EF structure in the presence of the actual catalytic ion, Mg^{2+}.[6] A two-ion binding site was obtained (Figure 2B) from a solution with inhibiting concentrations of Mg^{2+}.[6] However, substrate conformation and ion coordinations suggested an inactive structure.[7,9]

Structures 1K90 (with the ATP analogue) and 1SK6 (with products) also indicated that a histidine residue (His351) could act as the catalytic base, accepting a proton from ribose O3′.[3,4] However, the distances between the potentially reactive groups was large in ATP-analogue-bound models (Figure 2)—possibly because the ATP mimic used for crystallization lacked the

Received: March 10, 2016
Revised: May 23, 2016
Published: June 3, 2016

DOI: 10.1021/acs.jpcb.6b02527
J. Phys. Chem. B 2016, 120, 6504−6514

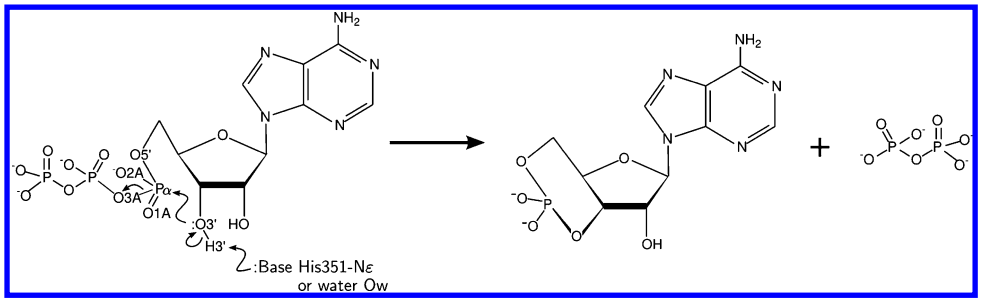

Figure 1. Schematic representation of the conversion of ATP into cAMP catalyzed by EF or mACs.

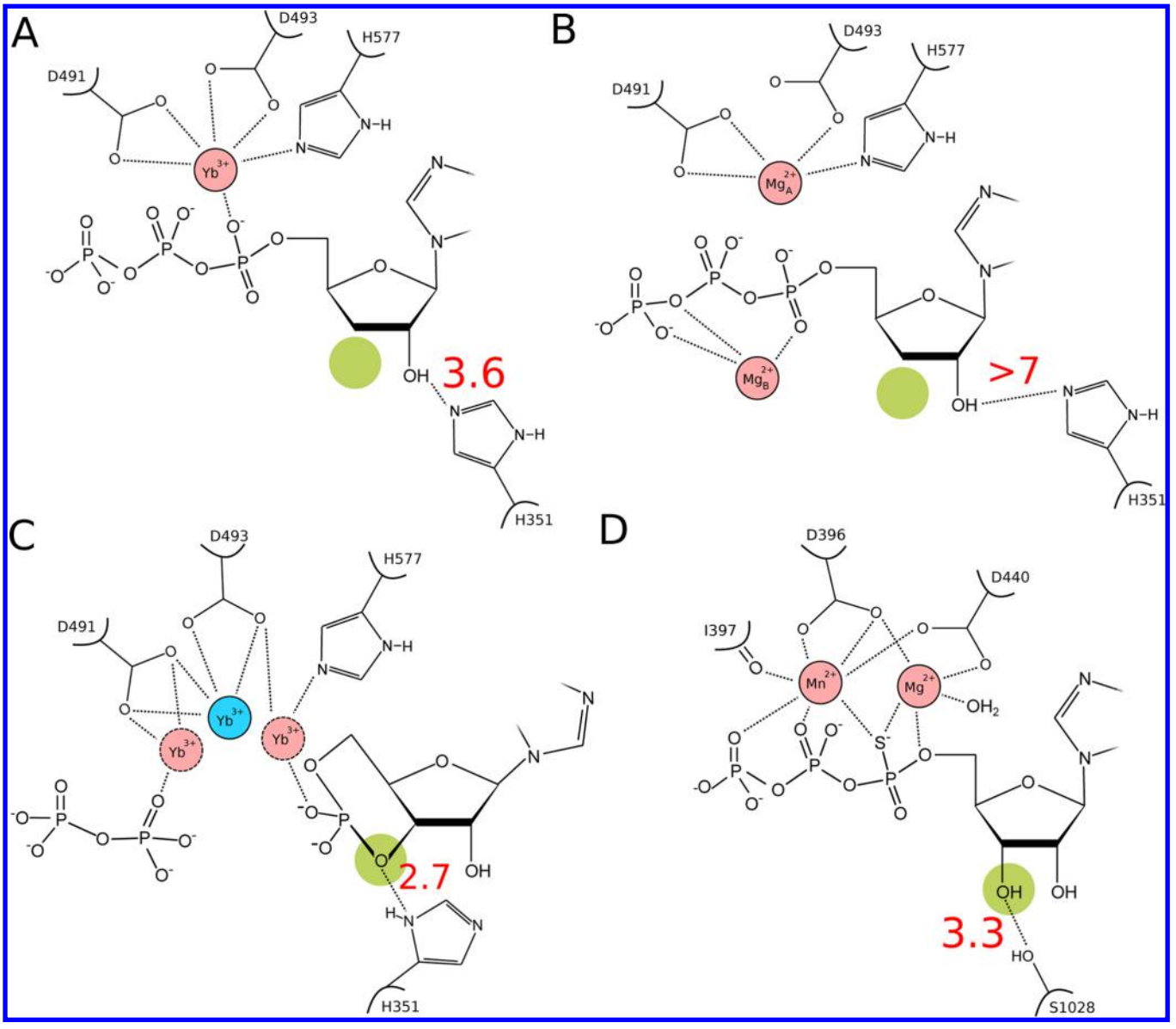

Figure 2. Schematic representation of the catalytic site organization observed in crystallographic models of (A, B, and C) EF and (D) mACs. Ion-coordination distances smaller than 3 Å are represented as dashed lines. The position of the O3′ nucleophilic oxygen is marked in green. It was lacking in the ATP analogues used to obtain EF substrate-bound models. (A) Structure of EF bound to an ATP analogue with one ion in the active site. (B) EF bound to an ATP analogue and two ions. (C) EF bound to reaction products with two different ion-binding modes. The position of His351 is consistent with its role as a base in the product-bound model but not in substrate-bound structures. (D) mAC bound to an ATP analogue.

reactive ribose hydroxyl.[6] Only in the product-bound structure is the His351-Nε atom close enough to the ribose O3′ to suggest a potentially reactive proton transfer.[4] Experimentally, the mutation of His351 to alanine knocks down EF activity. However, its mutation to lysine (H351K) causes only 2-fold slow-down in its activity (from 3500 to 1500 s^{-1}), and the optimum pH (8.5) does not change. Thus, His351 could help in increasing the local concentration of hydroxyl but would not

DOI: 10.1021/acs.jpcb.6b02527
J. Phys. Chem. B 2016, 120, 6504−6514

necessarily act as a general base.[6] Therefore, it is unclear if and how His351 acts as key residue responding to the highest catalytic rate of EF relative to mACs.

Therefore, a precise description of the EF reaction mechanism is needed, especially regarding ion-binding modes and the nature and role of the catalytic base. The EF crystallographic structures are also inconclusive about the reactive conformation of ATP. It is unclear, as a whole, how EF achieves such high reaction rates as compared to those of mACs.

A few computational studies were performed for describing the reaction mechanisms of EF and mACs.[8,10] Mones et al. performed a quantum mechanics−molecular mechanics (QM/MM) study of EF using the empirical valence bond method. They estimated the activation barrier of the two-metal ion-binding mode on the basis of two reaction proposals: the general base and the specific base mechanisms. The authors did not test the one-metal ion-binding mode due to computational limitations but argued that EF might be versatile enough to catalyze the reaction using both metal ion-binding modes.[8] Likewise, the mAC reaction mechanism was also studied using computational methods.[10] Hahn et al. explored different reaction pathways using QM calculations with a polarizable continuum model of solvation (PCM). A QM model represented the active site, and the PCM model, the rest of the system. Accurate activation energies for the catalytic reaction of a mAC were obtained but ignoring the entropic contributions of the rest of proteins and conformational variability of the active site.

Here, we propose a dynamical description of the catalytic mechanism of EF, mainly focused on determining the ion-binding mode of its active site. In addition, we were interested in finding the molecular basis for the large catalytic efficiency of EF. Free-energy profiles for EF and mAC catalyses were obtained by sampling nonequilibrium reaction paths with steered-molecular QM/MM simulations. We found that the reaction catalyzed by EF displays similar free-energy barriers in any of the two possible ion-binding modes and that intermediate states display greater conformational flexibility in EF than in mACs. Therefore, EF might adapt to different ion-binding modes and achieve higher catalytic rates by means of an entropic advantage. The molecular basis for these differences between EF and mACs are discussed.

MATERIALS AND METHODS

EF Structure. Two crystallographic models of the EF of anthrax were used for the simulations: (a) EF with one Mg^{2+} ion in the active-site (PDB id: 1K90)[3] and (b) EF enzyme with two Mg^{2+} ions in the catalytic site (PDB id: 1SK6).[4] 1K90 was obtained with EF bound to an ATP analogue (3′-deoxyadenosine-5′-triphosphate) that lacks the O3′ hydroxyl in the pentose moiety. ATP was formed by adding the lacking hydroxyl group to this inhibitor. The crystal structure of 1SK6 was solved in complex with reaction products cAMP and pyrophosphate. In both crystals, 1K90 and 1SK6, metal ions were present in the active site, which were identified as Yb^{3+} instead of the catalytically active Mg^{2+}. Therefore, we replaced the Yb^{3+} ions with Mg^{2+} ions.

mAC. The mAC crystallographic model, PDB id: 1CJK, was used.[5] The protein is a complex between the catalytic core of AC (which consists of two homologous cytoplasmic domains, C_{1a} and C_{2a}) and the α subunit of stimulatory G protein ($G_s\alpha$). The C_{1a} domain of the heterodimer complex is an AC type V from *Canis lupus*, whereas C_{2a} is an AC type II from *Rattus norvegicus*. The active site of AC was crystallized with an ATP analogue (adenosine-5′-rp-α-thio-triphosphate), one Mn^{2+} ion, and one Mg^{2+} ion. For the simulation, the Mn^{2+} ion was replaced by a Mg^{2+} ion. The complex is bound to a forskolin molecule, which is a terpene that helps in the stabilization of the heterodimer interface.[11] The crystal of the subunit $G_s\alpha$ was obtained with a GTP analogue (5′-guanosine-diphosphate-monothiophosphate) in its active site, which was replaced by GTP. The crystallographic structure lacks two loops: one in the C_{2a} subunit and the other in the $G_s\alpha$ subunit. The models of the missing loops were built using Modeller 9.14.[12] Ten refined loops for each model were generated, and the loop models with the most favorable DOPE energy were selected. The whole protein was kept rigid during loop modeling. The complete final structure was relaxed by molecular dynamics (MD) simulation.

Parametrization, Force Field, and Simulation Setup. The AMBER ff99sb force field was employed to describe the protein.[13] Ligands and cofactor molecules were modeled using the AMBER GAFF force field.[14] The parameters for describing ATP, Mg^{2+}, and H_3O^+ were taken from refs 15−17. GTP, cAMP, pyrophosphate, and forskolin structures were optimized using Gaussian09 with the B3LYP/6-311+G(d,p) level of theory.[18] The parameters for these ligands were determined by the antechamber program in the AMBER 14 package.[19,20] Partial charges of ligands were calculated using the AM1-BCC method.[21] Hydrogen atoms were modeled according to the most probable protonation state of each residue, that is, Asp and Glu were negatively charged and Lys and Arg were positively charged. Histidine protonation states were assigned favoring hydrogen bond formation. The protein was solvated in a box of TIP3P water molecules.[22] The final system dimensions were 157 × 108 × 108 Å. The systems contained about 180000 atoms. AmberTools15[20] and VMD were used for visualization and analysis.[23] The plots were generated using GNUPLOT and XMGRACE.

Classical MD. Energy minimization and equilibration simulations were performed with NAMD, which is convenient for performing MD simulations with fixed atoms.[24] All MD simulations were conducted under isobaric−isothermal conditions (NPT) at 300 K and 1 atm. Equilibrium runs were performed with temperature rescaling at every 100 fs, and Langevin pistons were used to control pressure at 1 atm with a coupling period of 0.2 ps and a decay of 0.1 ps. Periodic boundary conditions were used. Bonds involving hydrogen atoms were constrained to their equilibrium length using the RATTLE algorithm.[25] Electrostatic interactions were computed using the Particle Mesh Ewald (PME) method with a cutoff of 10 Å.[26,27] Equilibration was performed with the following protocol: (1) 2000 steps of conjugate-gradient energy minimization with all protein atoms, ligands, and active-site ions fixed, (2) 300 ps of MD with the same atoms fixed, for solvent relaxation, (3) 150 ps MD, fixing only the α-carbon atoms and active-site atoms (ATP, Mg^{2+}, coordination sphere, and base), (4) 100 ps MD, fixing only α-carbon atoms of the protein, and (5) 100 ps MD without restraints. Production runs were 15 ns long and were performed using the PMEMD program, which is part of the AMBER 14 package.[20,28] In this case, the temperature was set to 300 K and the pressure to 1 atm using the Berendsen thermostat and barostat, with coupling constants of 2 and 1 ps, respectively.[29] A 2 fs time step was used, and bonds involving hydrogens were constrained

DOI: 10.1021/acs.jpcb.6b02527
J. Phys. Chem. B 2016, 120, 6504−6514

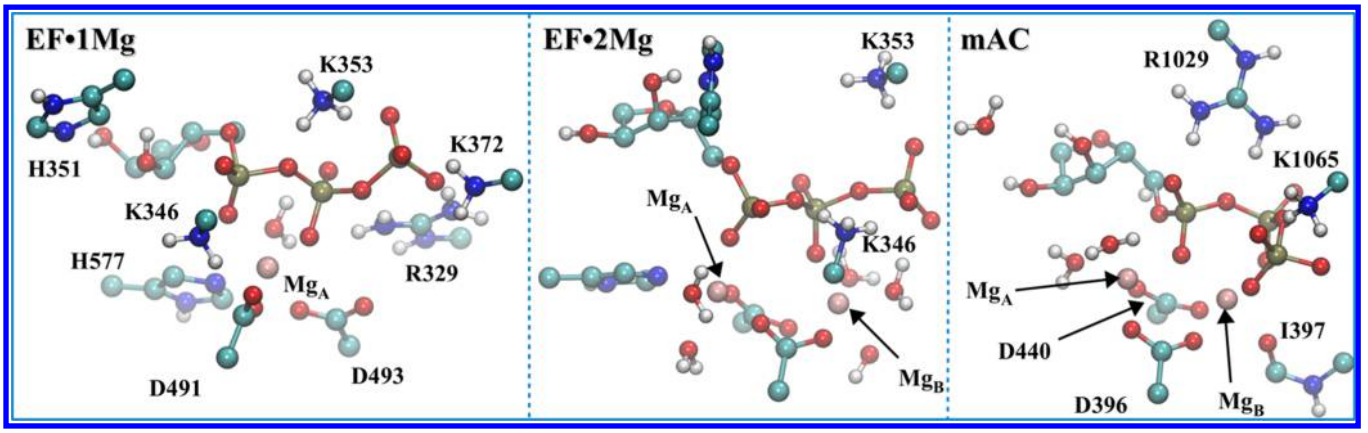

Figure 3. QM region used in the QM/MM simulations for EF with one or two Mg^{2+} ions (EF·1Mg and EF·2Mg, respectively) and for the mAC. Only heavy atoms and polar hydrogens are shown.

with SHAKE.[30] A cutoff of 10 Å was used for nonbonded interactions, and electrostatic interactions were computed using the PME method. The classical production simulation was used to select representative frames for the QM/MM/multiple-steered molecular dynamics (MSMD) simulations.

Reaction Coordinate. The reaction involves a phosphoryl transfer and a proton transfer (Figure 1). Phosphoryl transfer was described by the O3A−Pα and O3′−Pα distances (Figure 1). Proton transfer was described by the distances between ribose atoms O3′ and H3′ and between ribose-H3′ and His351-Nε or water-Ow atoms. We used the −d(O3′−Pα) + d(O3A−Pα) − d(H3′−Nε/Ow) reaction coordinate. An alternate reaction coordinate which included explicitly the O3′−H3′ distance was considered, but this inclusion proved to be unnecessary and apparently decreased the rate of productive trajectories.

QM/MM Simulations. The QM/MM simulations were performed with a modified version of Sander program from the AMBER12 package[31] in which the HyDRA algorithm on MSMD simulations is implemented.[32,33] This algorithm significantly improves the convergence of the free-energy profiles obtained from nonequilibrium trajectories. The quantum mechanical level used was the semiempirical density-functional-based tight-binding (DFTB) method using the self-consistent charge (SCC) approach[34−36] as implemented in the sander module of AMBER.[37] SCC−DFTB parameters were obtained from ref 36 and were used with second-order corrections. The use of third-order PR extension results in instabilities in the calculations of the Amber QM module and, therefore, were not used. The SCC−DFTB parameter for Mg^{2+} was provided by Prof. Quiang Cui and consists of the parameters reported in ref 35. Lysine and arginine residues were included in the QM subsystem to neutralize the total QM charge (Figure 3). The MM region was modeled with the AMBER ff99SB force field. The simulations were run using periodic boundary conditions and PME electrostatics, for both regions. The electrostatic cutoff was set to 15 Å.

Free-Energy Profiles. The forward and backward free-energy profiles were obtained from MSMD simulations and the application of the Jarzynski nonequilibrium equality for free-energy differences (parts A and B in Figures S1−S3).[38,39] The free-energy profiles of the reaction were obtained by a combination of the forward and backward free-energy profiles of the reaction (parts C and D in Figures S1−S3). Each MSMD simulation consisted of 48 000 QM/MM steps, with a pulling speed of 0.5 Å ps^{-1}, using a Differential Relaxation Algorithm ratio of 4,[32] a force constant of 300 kcal mol^{-1} $Å^{-2}$, and a time step of 1 fs.[32] The configurations used for MSMD simulation were selected from classical MDs. Therefore, frames were QM/MM-optimized, with 2000 steepest descent iterations, and equilibrated for 30 ps at the QM/MM level before productive runs. All of the QM/MM simulations were performed in a canonical ensemble. The temperature was set to 300 K using a Berendsen thermostat[29] with a coupling constant of 2 ps. At least 30 independent MSMD simulations were used to build each free-energy profile (forward or backward). Harmonic restrictions were applied for N−H bonds of lysines and arginines and for the O−H bond of the second pentose hydroxyl group to avoid undesirable side reactions. A harmonic restriction of 100 kcal mol^{-1} $Å^{-2}$ was used to restrain the Mg−Nε_{H577} distance to 2.5 Å in EF systems, to preserve the coordination sphere observed in the crystallographic model. Restrictions were introduced to keep water molecules in place whenever necessary. The error of the free-energy estimates was computed assuming the independence of each trajectory. It was estimated by computing the standard error of the Jarzynski exponential mean, propagated to first order to the free energy.

DFT Corrections on Free-Energy Barriers. SCC−DFTB is a semiempirical method based on DFT. It reproduces geometries which are in good agreement with those obtained with DFT and is reliable for obtaining structural properties for metal sites and reaction dynamics. We applied higher-level QM corrections to estimate the dependence of free-energy estimates with the level of theory. Two DFT functionals were used, B3LYP[40,41] and M06.[42] The basis set used was 6-31G(d). B3LYP was selected because it produces structures in good agreement with MP2 for phosphate reaction hydrolysis.[36] M06 is recommended to study the thermodynamics for both main group elements and transition metals.[42,43] The correction of free energies, $\Delta G_{DFTB\rightarrow DFT}$, is obtained as suggested in ref 44, using the following thermodynamic cycle:

DOI: 10.1021/acs.jpcb.6b02527
J. Phys. Chem. B 2016, 120, 6504−6514

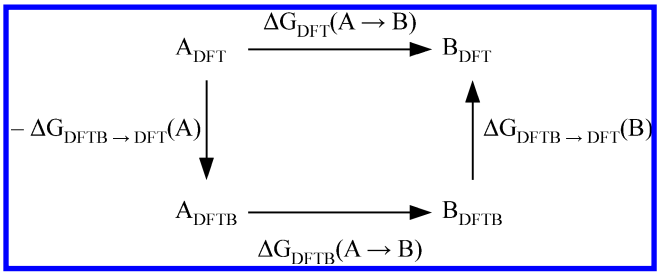

The free energies of steps A and B were calculated using a one-step free-energy perturbation (FEP) scheme. When the computation is performed for the forward reaction, states A and B are the reactants and the transition state, respectively. A and B are the products and the transition state, respectively, if the activation free energy of the backward reaction is considered. This strategy is based on the idea that the structures of the QM subsystem of reactants, products, and transition states can be satisfactorily obtained with a lower-level QM method. Thus, the QM corrections were applied by performing QM/MM single-point calculations using a higher-level theory on representative SCC−DFTB structures obtained from a QM/MM MD simulation. The QM/MM single-point calculations used DFT and electrostatic embedding and were performed using an Amber interface[45] to external QM software package. In this case, Gaussian09 was used.[18] Then, the free-energy differences provided by each method are obtained using a Free-Energy Perturbation approach, in which the sampling of conformations is performed only for the classical part, with the SCC−DFTB structure of the QM subsystem fixed[46−48]

$$\Delta G_{DFTB \rightarrow DFT} = -RT \ln \left\langle \exp\left[\frac{-(U_{DFT} - U_{DFTB})}{RT}\right]\right\rangle_{DFTB}$$

We estimated these differences for the reactants, transition states, and products of the SMD trajectories of lowest energy. The correction was computed using at least 250 snapshots extracted every 1 ps from 15 independent QM/MM MD simulations in which the QM subsystems were fixed. Convergence of the correction was observed after ∼200 snapshots. Ideally, the correction should be computed for all reactant, product, and transition-state structures obtained with SCC−DFTB, but this would be computationally prohibitive. The obtained estimates, using only the lowest-energy SCC−DFTB curves, are only indicative of the nature of correction that a higher level of theory would provide. Similar schemes were applied to adjust free-energy values from semiempirical methods[49,50] and MM methods to higher-level QM.[51,52]

RESULTS AND DISCUSSION

Free-Energy Profiles. Figure 4 displays the free-energy profiles of the reactions catalyzed by EF with one and two Mg^{2+} and for the mAC (with two Mg^{2+}). In EF, His351 is considered as the catalytic base, removing the ribose H3′ proton. There is no His351 counterpart in mACs; therefore, a water molecule was used as the catalytic base for proton abstraction. The free-energy barriers for the forward reaction catalyzed by EF were similar in both ion-binding modes, of the order of 22−24 kcal mol^{-1}. On the basis of these results, EF would be able to catalyze the reaction in the presence of one or two ions with similar rates. This is consistent with the experimental observation that EF activity is close to maximal in a wide range of Mg^{2+} concentrations,[9] suggesting an adaptation of this enzyme to different environmental conditions. On the other hand, the activation barrier of the reaction catalyzed by the mAC is significantly greater (33 kcal mol^{-1}; see Figure 4). The difference in activation free energies between EF and the mAC is in qualitative agreement with the higher catalytic rate of EF.[4]

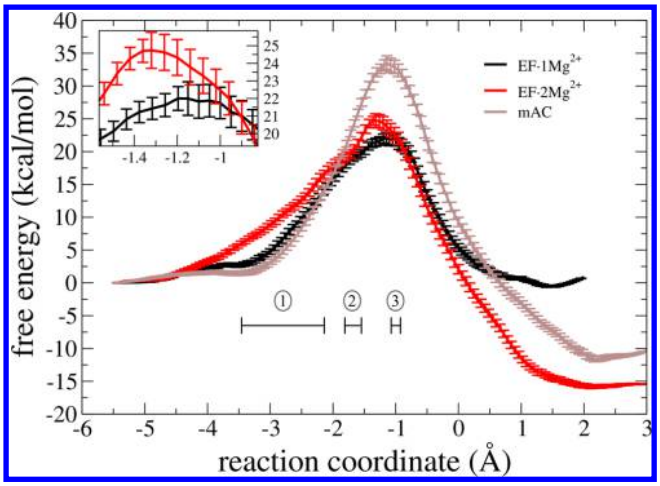

Figure 4. Free-energy profiles for the conversion of ATP into cAMP catalyzed by EF and a mAC. The activation energy is higher for the mAC, consistently with the higher catalytic efficiency of EF. Activation energy for EF is only marginally dependent on the ionic content of the active site, but the presence of two ions greatly stabilizes reaction products. Labels 1 and 2 indicate the reaction coordinate ranges in which proton transfer occurs in EF and the mAC, respectively. Label 3 indicates the reaction coordinate of phosphate transfer in all systems.

In the presence of two metal ions, the reaction products are notably stabilized relative to the substrates, both for EF and the mAC. The stabilization of the products is of ∼16 kcal mol^{-1} for EF and ∼12 kcal mol^{-1} for the mAC (Figure 4 and Table 1).

Table 1. Estimates of the Free-Energy Parameters of the Reaction, Using SCC−DFTB (All Values in kcal mol^{-1})[a]

system	$\Delta G°$	$\Delta_f G^{\#}$	$\Delta_b G^{\#}$
EF·1Mg	−0.5 (1.6)	22.0 (0.6)	22.1 (1.0)
EF·2Mg	−15.8 (1.9)	24.1 (0.9)	40.6 (1.0)
mAC	−11.6 (1.4)	33.4 (0.9)	45.1 (0.5)

[a] $\Delta G°$: overall reaction free energy; $\Delta_f G^{\#}$: activation free energy of the forward reaction. $\Delta_b G^{\#}$: activation free energy of the backward reaction. The estimated deviations are in parenthesis and are computed as described in the Materials and Methods section.

This implies that backward reactions are, in the presence of two ions, slower than the corresponding forward reactions. This is consistent with the experimentally known rates for forward and backward reactions: For mACs, the forward reaction is 30 times faster than the backward reaction, consistently with the stabilization of the reaction products in the two-metal-ion active site.[53] By contrast, EF displays similar forward and backward reaction rates, as reported in ref 4. In our simulations, there is virtually no free-energy difference between substrate and reaction products in the single-Mg^{2+} EF mechanism. Therefore, this fundamental difference between EF and mACs might be explained by the possibility of EF catalyzing the reaction with a single ion.

As the nature of the base can play an essential role in the reaction free energy, we studied the EF·2Mg system assuming a water molecule as the base. However, we could not obtain consistent ATP-H3′ transfers to water. Furthermore, the

DOI: 10.1021/acs.jpcb.6b02527
J. Phys. Chem. B 2016, 120, 6504−6514

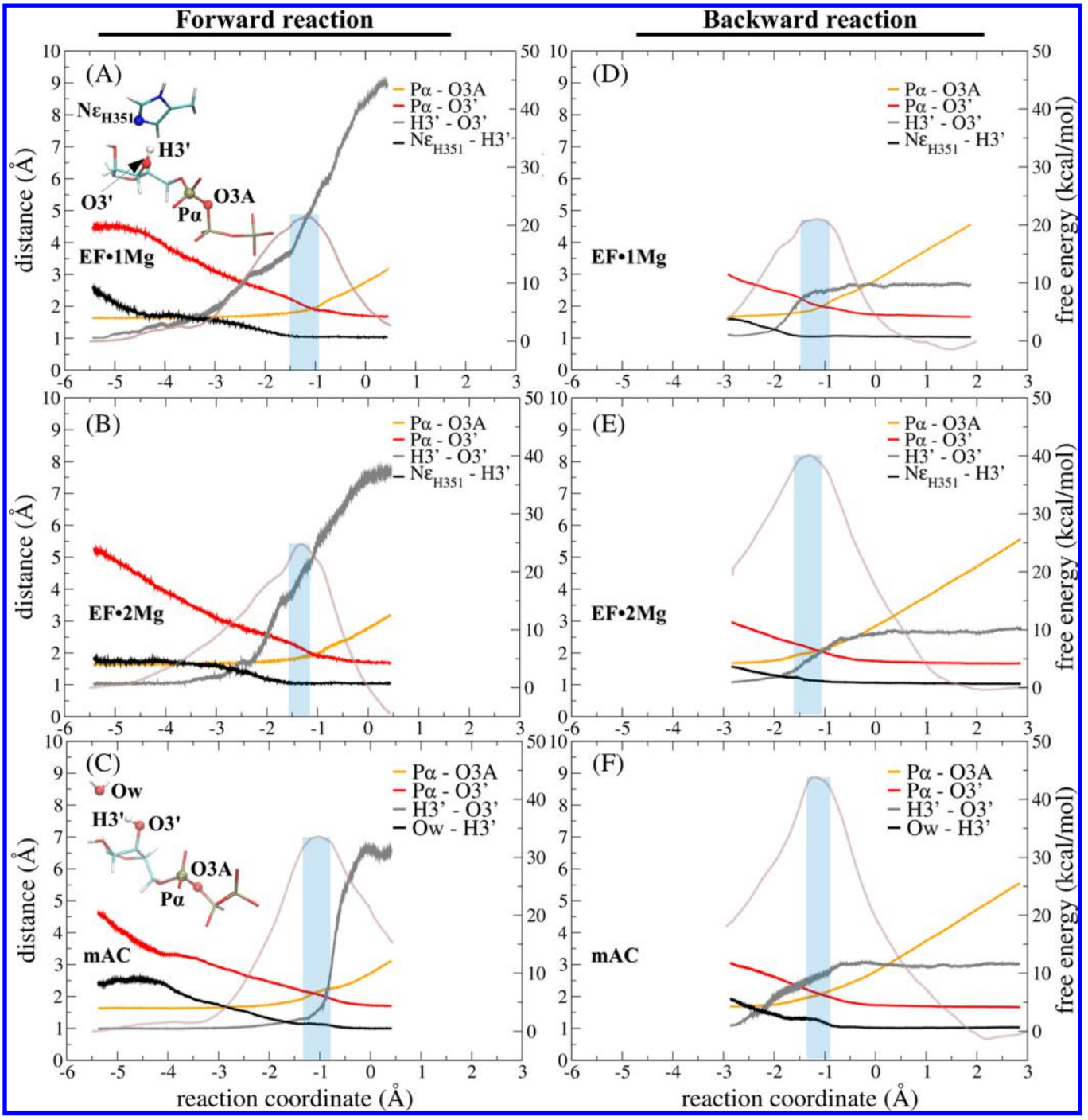

Figure 5. Distances involved in proton transfer and phosphate transfer for (A and D) EF·1Mg, (B and E) EF·Mg, and (C and F) the mAC. The distances are as follows: (His351)Nε−H3′, H3′−O3′, Pα−O3A, and Pα−O3′ (black, gray, orange, and red lines, respectively). In the molecular representation, the atoms involved are shown in CPK. The first two distances describe proton transfer and the last two, phosphate transfer. Proton transfer takes place at the crossing point between the gray and black lines. Phosphate transfer takes place at the intersection between the orange and red lines. Brown curves show the forward or backward free-energy profiles for each system, and the blue bar indicates the transition state region. Plots A−C concern the forward reaction, and D−F, the backward reaction.

smaller works obtained for the trajectories under all conditions tested were higher than 30 kcal mol^{-1} (Figure S4). This result supports the conclusion that His351 is essential for the reaction.

Therefore, the transition-state free energies obtained are in qualitative agreement with the experimental reaction rates. However, the actual experimental barriers are much smaller. The experimental kinetic parameters available, extrapolated to transition state energies through the Eyring equation, indicate that the transition state free energies for the forward reaction are ∼15[53] and 13−14[3,4,54] kcal mol^{-1} and for the backward reaction are ∼17[53] and 14−15[3,4,54] kcal mol^{-1} for the mAC and EF, respectively. Because SCC−DFTB is not as accurate as ab initio methods to reproduce experimental values, the activation free energies were recomputed using one-step free-energy perturbation with a higher-level QM method (see Table

DOI: 10.1021/acs.jpcb.6b02527
J. Phys. Chem. B 2016, 120, 6504−6514

Table 2. Geometric Parameters of the Transition States[a]

system	RC at TS	d(O3′−Pα) (Å)	d(Pα−O3A) (Å)	ψ(PO_3) (deg)	θ(OPO) (deg)
EF·1Mg	−1.20	2.01 (0.08)	1.84 (0.06)	−1.58 (3.17)	171.6 (3.84)
		2.05 (0.13)	1.88 (0.10)	−1.56 (3.38)	171.4 (4.28)
EF·2Mg	−1.30	2.12 (0.11)	1.85 (0.09)	−4.30 (3.92)	171.8 (3.67)
		2.15 (0.12)	1.99 (0.21)	0.02 (3.24)	171.1 (4.44)
mAC	−1.12	2.01 (0.12)	2.09 (0.21)	−0.60 (3.26)	172.7 (4.36)
		2.09 (0.20)	2.07 (0.24)	2.51 (4.52)	170.5 (3.96)

[a]RC: reaction coordinate at the transition state; d(O3′−Pα): distance between O3′ and Pα (forming bond in the forward reaction); d(Pα−O3A): distance between Pα and O3A (breaking bond in the forward reaction); ψ(PO3): improper dihedral angle of the phosphate moiety (O2A−O5′−O1A−Pα); θ(OPO): O3′−Pα−O3A angle. The first and second values in each cell correspond to the forward and backward reactions, respectively. The standard deviations of the means are shown in parentheses.

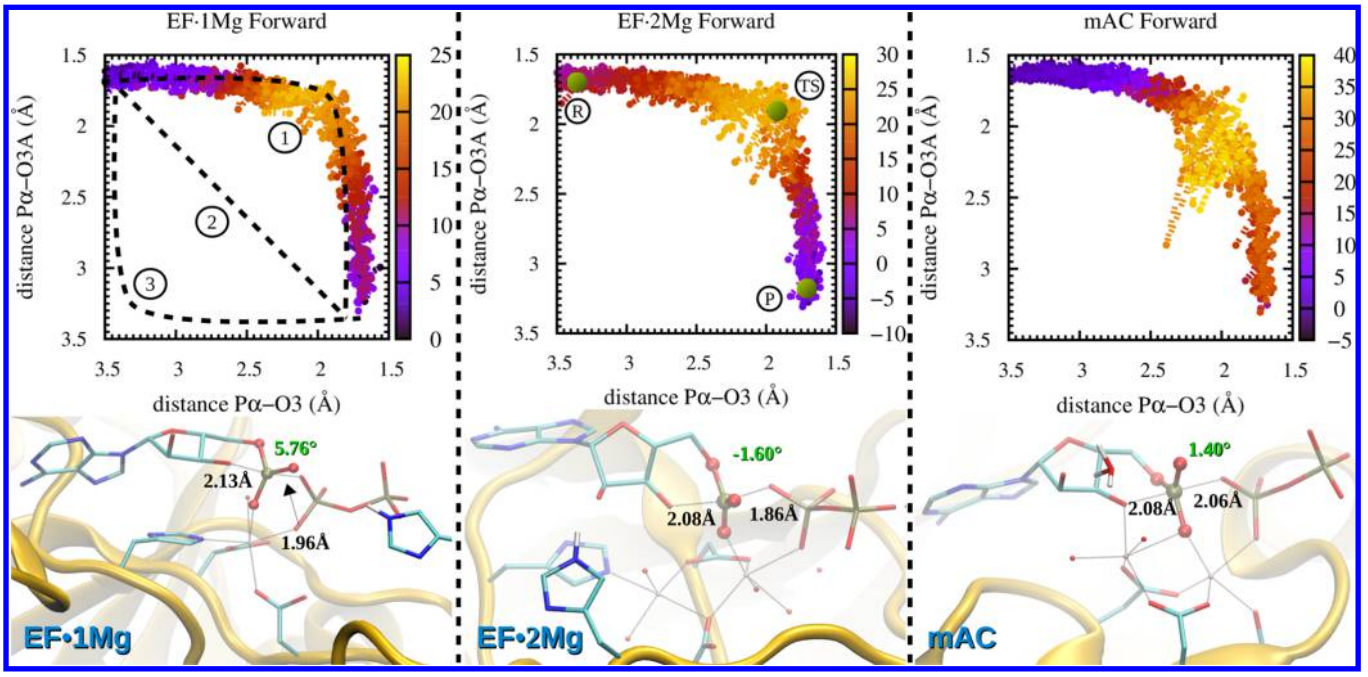

Figure 6. On top: More-O'Ferrall−Jencks diagram of bond formation (*x*-axis) and bond breaking (*y*-axis) for EF·1Mg, EF·2Mg, and the mAC. Labels 1, 2, and 3 represent the typical examples for associative, concerted, and dissociative mechanisms, respectively. The EF reaction is highly associative, according to our results. Labels R, TS, and P represent the locations of reactants, transition states, and products. On bottom: transition state structures for EF·1Mg, EF·2Mg, and the mAC. The distances involved in phosphoryl transfer (black) and the improper dihedral angle of the phosphoryl group (green) are indicated.

S1).[48,55] Unfortunately, as here the QM subsystem is fixed, this methodology has an important limitation that its entropy is not taken into account.[44] As we will see, this component appears to be essential for the EF mechanism. All free-energy barriers decreased in the FEP calculations relative to SCC−DFTB, as reported in Table S1. The barriers became closer to experimental free-energy barriers. The more-accurate relative free energies of the reactions supported the conclusions obtained from SCC−DFTB calculations that are as follows: (1) EF is more efficient than mACs in both ion-binding modes. (2) The two-metal ion-binding mode stabilizes reaction products relative to reactants, thus reducing the rate of reverse reaction. At the same time, these new estimates might indicate that EF with two ions is more efficient than that with a single ion. Similar results were obtained using M06 and B3LYP (see Table S1).

Description of the Mechanism. The reaction catalyzed by ACs involves a proton and a phosphoryl transfer. The phosphoryl transfer depends on the attack of the ATP-O3′ oxygen to Pα and the rupture of the Pα−O3A bond. The formation of the O3′−Pα bond is dependent on the transfer of the proton bound to O3′ (H3′) to some base. Here, His351 is considered as the catalytic base in EF. A water molecule is considered as the catalytic base in the mAC (Figures 4 and 5). The proton transfer is described by distances d($N\varepsilon_{H351}$/Ow−H3′) and d(H3′−O3′). Likewise, the phosphoryl transfer is represented by two distances: d(Pα−O3′) and d(Pα−O3A). Proton and phosphate transfers occur at the crossing points of each pair of distances (when the forming bond has the same distance as the breaking bond). Therefore, in Figure 5, phosphoryl transfer occurs at the crossing point of the orange and red lines, and proton transfer occurs at the crossing point of the black and gray lines. The mechanisms are similar for the three systems, except for the nature of the catalytic base. Proton abstraction from O3′ precedes phosphate transfer (Figure 5). For EF, proton abstraction takes place earlier than for the mAC and also in a greater range of reaction coordinates (Figure 4 and 5). This variability was observed in both directions (see Figure 5). Therefore, our results suggest that the EF mechanism involves an earlier proton transfer than that in

DOI: 10.1021/acs.jpcb.6b02527
J. Phys. Chem. B 2016, 120, 6504−6514

mACs. In the mAC mechanism, the O3′ ribose oxygen systematically coordinates to Mg^{2+} at the A-site (Mg_A) before proton transfer. Finally, in EF·2Mg, a water molecule (coordinated to the Mg_A ion) stabilizes the negative charge emerging on the O3′ oxygen by temporarily transferring a proton to it (described in more detail in the Charge Analysis section). This was not observed for EF·1Mg.

Two-metal-aided catalysis is involved in many enzymatic phosphoryl-transfer reactions. In these enzymes, the cooperative motion of the two ions appears to be an important feature of reaction mechanism. For instance, De Vivo et al. described a cooperative motion of Mg^{2+} ions in Ribonuclease H. The distance between the two ions decreases from 4.1−4.2 Å in the reactant state to 3.8−3.9 Å in the transition state, and it is restored in the product state.[56,57] Similar cooperative movements were observed here for EF·2Mg, as shown in Figure S5. The interionic distance decreases from ∼4.2 Å in reactants to ∼3.5 Å in the transition state, being restored to ∼4.0 Å in the products. However, the ion distances in the mAC did not display the same behavior. The distance between the ions (∼3.5 Å) is smaller than that in EF·2Mg (4.2 Å) and increases slightly along the reaction, reaching ∼3.75 Å in the products (see Figure S5).

Ion coordination can also be essential in enzymatic phosphoryl-transfer reactions.[57,58] In our simulations of EF·2Mg, both ions display stable octahedral coordination along the reaction (Figure S6). The same happens with the Mg_A ion in the mAC. However, the Mg^{2+} ion in the B-site of the mAC (Mg_B) is hexacoordinated in the reactant state and becomes pentacoordinated (with trigonal bipyramidal geometry) at the transition state. This occurs because one of the Pγ oxygen atoms leaves the ion coordination sphere. In the mAC product state (Figure S6), the coordination of the ions is noncanonical: a water molecule interacts with both ions, coordinating more tightly the one at the A-site.

Associative Character of the Reaction and Description of the Transition State. The conversion of ATP into cAMP consists of a phosphoryl transfer reaction. This kind of reaction may be associative, dissociative, or concerted.[59] One way to determine the associative/dissociative (A/D) character of the reaction mechanism is measuring the O−P distances at the TS. The A/D percentage is determined by correlating the bond distance to the fractional bond number from Pauling.[60] Therefore, an analysis of transition states was performed using the average distances of the transition-state structures of all of the productive trajectories (Table 2). The transition state is located in the region where the phosphate moiety is transferred, occurring after proton transfer, as discussed. The distances that characterize phosphate transfer in the transition state are as follows: Pα−O3′ = 2.0 Å and Pα−O3A = 1.9 Å (Table 2). The proximities of Pα and O3′ suggest that the reactions are associative, in all cases.[60] The improper dihedral angle (defined by O2A−O5′−O1A−Pα) of the phosphate was close to 0°, as expected for the transition states of S_N2 reactions. In addition, the angle formed between the breaking and forming bonds (O3′−Pα−O3A) is close to 170°. Figure 6 shows a representative structure of the transition state ensemble for each system.

To confirm the associative character of the reactions, we computed More-O'Ferrall−Jencks diagrams. These diagrams are two-dimensional plots of the free-energy surface as a function of the two O−P distances associated with phosphate transfer.[59] The first panel of Figure 6 depicts the three different mechanistic possibilities. Label "1" indicates an associative mechanism in which the O3′ (nucleophilic atom) approaches Pα before the Pα−O3A bond starts breaking, forming a phosphorane group in the limiting case. The completely opposite scenario is labeled "3", in which the Pα−O3A bond is broken before the formation of the O3′−Pα bond, resulting in a metaphosphate TS structure. Finally, label "2" represents a concerted mechanism, in which the formation and breaking of phosphate bonds are simultaneous, that is, O3′−Pα is formed at the same time when Pα−O3A is broken.[59] In the present work, all reactions were observed to be highly associative, such that transition states display clearly distinguishable pentacoordinated Pα phosphate groups (Figure 6). This result is in agreement with the description of the transition state structure described in ref 8.

Conformational Flexibility of the Transition States. In a previous work, classical MD simulations of EF structures suggested that the flexibility of the active site, including ATP and ions, could play an important role in the catalytic efficiency.[7] ATP was observed to display different flexibilities depending on the crystallographic model used. Here, we performed an analysis of the flexibility of the transition state in EF and mACs (Figure 7). The structure of the transition state displays greater conformational flexibility in EF than that in the mAC, specially in the ribose and phosphate groups (Figure 7B). The conformational variability of the TS structure in mACs is much smaller than that in EF, as a consequence of the limited mobility of the O3′ oxygen, which is tightly coordinated to the Mg^{2+} ion. This coordination increases O3′−H3′ acidity, assisting proton transfer to the water molecule acting as a base. However, it restricts the conformational flexibility of the substrate, hence resulting in an entropic penalty. EF appears to retain its catalytic efficiency even with a looser attachment of the ribose oxygen to the ion because the proton transfer is assisted by His351, which is more basic than water. Therefore, a greater conformational flexibility of the transition state of EF might allow the sampling of lowest-energy structures and possibly increases TS entropy.

Charge Analysis. The charges of the QM subsystems were computed along the reaction coordinate. The ribose O3′ has a greater (less-negative) charge in the mAC than in EF·2Mg (Figure S7) because it shares part of its negative charge with the Mg_A ion (Figure 8). This is in agreement with the tight coordination of the O3′ to the Mg_A ion described above for the mAC. The Mg_A ion itself is less positive in EF possibly because of the coordination of the His577 residue. The greater charge of the O3′ oxygen in the mAC contributes to a greater acidity of the H3′ proton, allowing its effective transfer to water molecules.

In EF, residues K346 and K353 take some of the negative charge of the phosphates, likely stabilizing the transition state (Figures S8 and S9). In the case of the mAC, the residues R1029 and K1065 participate in the reaction by stabilizing the reactants, but only R1029 seems to interact with the transition state (Figure S10). Interestingly, these residues are part of the C_{2a} monomer that conforms with the heterodimer complex, but the residues that participate in the coordination of the Mg^{2+} ions are part of another unit, C_{1a} (the catalytic core of this mAC consists of two homologous cytoplasmic domains: C_{1a} and C_{2a}[5]). This is in agreement with the fact that the active site is shared between the two monomers and their association is necessary for the catalytic activity of the mAC.[61,62]

DOI: 10.1021/acs.jpcb.6b02527
J. Phys. Chem. B 2016, 120, 6504−6514

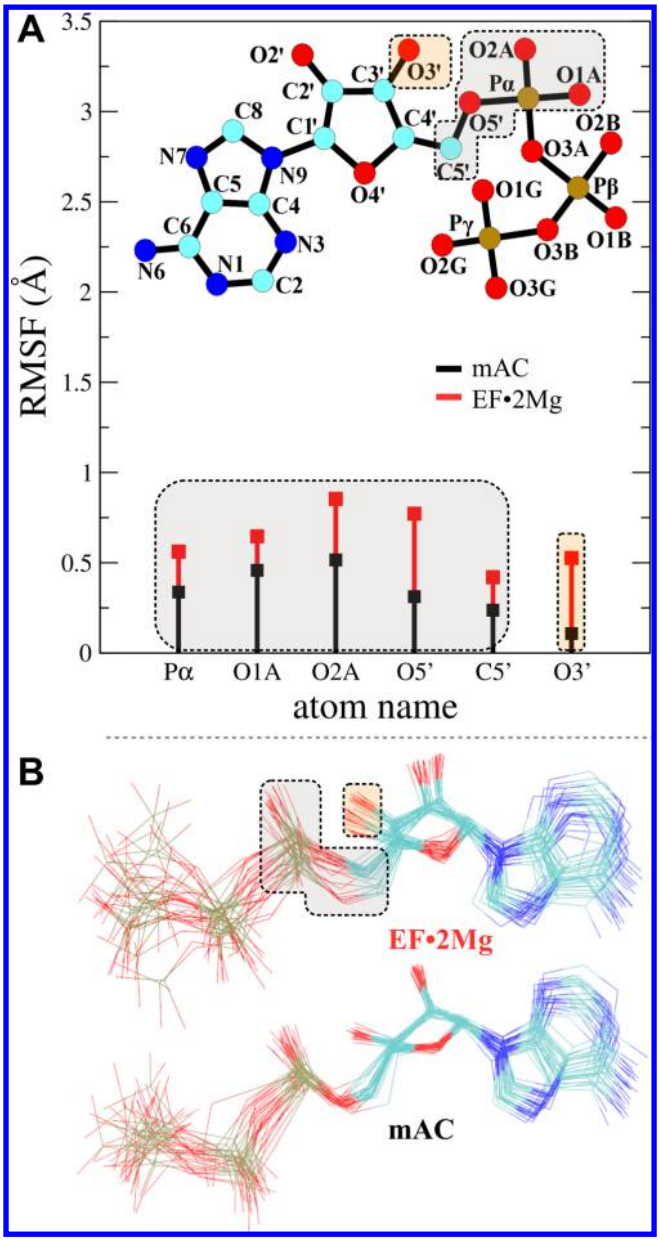

Figure 7. Conformational variability of the transition state structures of EF·2Mg and the mAC: (A) Flexibilities (computed as RMSFs) of the transferring phosphate and ribose (for simplicity, only C5′ and O3′ are shown). (B) Conformational diversity of the transition state structures of EF and the mAC. The increased flexibility of the substrate in EF facilitates the approach of O3′ to Pα and possibly the sampling of lower-energy conformations.

The evolution of charges in EF·2Mg also reveals the participation of a water molecule, coordinated to the Mg_A ion, in the reaction. After H3′ is transferred to His351, this water molecule (which is acidic because of its coordination to the ion) gains electron density, and its charge goes from positive ($+0.2e^-$) to negative ($-0.2e^-$). This occurs because of the temporary transfer of one of its protons to the O3′ atom of ATP .

CONCLUSIONS

We have performed QM/MM calculations to address fundamental questions about the catalysis mechanism of the EF of anthrax. Our calculations indicate that EF can catalyze the reaction in any of the two ion-binding modes, a solution to the controversy of the number of ions present in the EF active site. This mechanistic flexibility might be an adaptation to ion availability of infected host cells. Given the accuracy of our calculations, we cannot rule out the possibility that rates of catalysis are greater with two Mg^{2+} ions in the EF, but there is enough evidence to assert that EF displays higher catalytic rates than mACs in both ion-binding modes. EF can be more efficient than mACs because the binding site ion is not required for proton abstraction from the ribose O3′ hydroxyl. Indeed, EF appears to avoid this interaction by having an additional basic residue to coordinate the catalytic ions. The reduced acidity of the O3′ oxygen is compensated by the presence of the basic His351 residue that can act as a general base. Indirectly, the looser attachment of the substrate to the ions allows for a greater conformational flexibility of the transition state, possibly favoring the reaction via entropy.

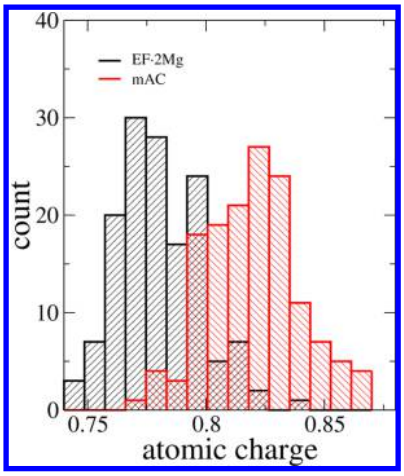

Figure 8. Mulliken charge distributions of the Mg^{2+} ions coordinated to O3′ in EF·2Mg (black) and in the mAC (red). The histogram represents the charges at the reactant region of the reaction coordinate, averaged over the three SMD trajectories of smaller works. The figure shows that the ion charge is more positive in the mAC than in EF·2Mg, increasing the acidity of the coordinated O3′.

ASSOCIATED CONTENT

Supporting Information

The Supporting Information is available free of charge on the ACS Publications website at DOI: 10.1021/acs.jpcb.6b02527.

Table S1 with FEP estimates of free energies; Figures S1−S3 showing the construction of free-energy profiles; Figure S4 showing the tentative simulations using water as a base in EF; Figure S5 with Mg^{2+}−Mg^{2+} distances in EF and the mAC; Figure S6 describing the coordination of Mg^{2+} ions; Figure S7 with charges and distances involving Mg^{2+} and O3′; and Figures S8−S10 showing charges of residues involved in the reaction mechanisms (PDF)

AUTHOR INFORMATION

Corresponding Author

*E-mail: leandro@iqm.unicamp.br.

Notes

The authors declare no competing financial interest.

DOI: 10.1021/acs.jpcb.6b02527
J. Phys. Chem. B 2016, 120, 6504−6514

■ ACKNOWLEDGMENTS

The authors thank FAPESP and the Center for Computational Engineering and Sciences (CCES) (grants 2010/16947-9, 2013/08293-7, 2013/05475-7, and 2013/22360-9), CNPq (grant 470374/2013-6), and FAEPEX (grant 596/13) for financial support. The authors also thank Prof. Qiang Cui (University of Wisconsin, Madison) for providing the parameters we used for SCC-DFTB calculations. We specially thank Prof. Marcelo A. Martí (University of Buenos Aires) for helpful discussion and for the HyDRA code.

■ REFERENCES

(1) Mock, M.; Fouet, A. Anthrax. *Annu. Rev. Microbiol.* **2001**, *55*, 647−671.
(2) Dixon, T.; Meselson, M.; Guillemin, J.; Hanna, P. Anthrax. *N. Engl. J. Med.* **1999**, *341*, 815−826.
(3) Drum, C. L.; Yan, S.-Z.; Bard, J.; Shen, Y.-Q.; Lu, D.; Soelaiman, S.; Grabarek, Z.; Bohm, A.; Tang, W.-J. Structural Basis for the Activation of Anthrax Adenylyl Cyclase Exotoxin by Calmodulin. *Nature* **2002**, *415*, 396−402.
(4) Guo, Q.; Shen, Y.; Zhukovskaya, N. L.; Florian, J.; Tang, W.-J. Structural and Kinetic Analyses of the Interaction of Anthrax Adenylyl Cyclase Toxin with Reaction Products cAMP and Pyrophosphate. *J. Biol. Chem.* **2004**, *279*, 29427−29435.
(5) Tesmer, J. J. Two-Metal-Ion Catalysis in Adenylyl Cyclase. *Science* **1999**, *285*, 756−760.
(6) Shen, Y.; Zhukovskaya, N. L.; Guo, Q.; Florián, J.; Tang, W.-J. Calcium-Independent Calmodulin Binding and Two-Metal-Ion Catalytic Mechanism of Anthrax Edema Factor. *EMBO J.* **2005**, *24*, 929−941.
(7) Martínez, L.; Laine, E.; Malliavin, T. E.; Nilges, M.; Blondel, A. ATP Conformations and Ion Binding Modes in the Active Site of Anthrax Edema Factor: A Computational Analysis. *Proteins: Struct., Funct., Bioinf.* **2009**, *77*, 971−983.
(8) Mones, L.; Tang, W.-J.; Florián, J. Empirical Valence Bond Simulations of the Chemical Mechanism of ATP to cAMP Conversion by Anthrax Edema Factor. *Biochemistry* **2013**, *52*, 2672−82.
(9) Shen, Y.; Lee, Y.-S.; Soelaiman, S.; Bergson, P.; Lu, D.; Chen, A.; Beckingham, K.; Grabarek, Z.; Mrksich, M.; Tang, W.-J. Physiological Calcium Concentrations Regulate Calmodulin Binding and Catalysis of Adenylyl Cyclase Exotoxins. *EMBO J.* **2002**, *21*, 6721−32.
(10) Hahn, D. K.; Tusell, J. R.; Sprang, S. R.; Chu, X. Catalytic Mechanism of Mammalian Adenylyl Cyclase: A Computational Investigation. *Biochemistry* **2015**, *54*, 6252−6262.
(11) Bier, D.; Thiel, P.; Briels, J.; Ottmann, C. Stabilization of Protein-Protein Interactions in Chemical Biology and Drug Discovery. *Prog. Biophys. Mol. Biol.* **2015**, *119*, 10−19.
(12) Šali, A.; Blundell, T. L. Comparative Protein Modelling by Satisfaction of Spatial Restraints. *J. Mol. Biol.* **1993**, *234*, 779−815.
(13) Hornak, V.; Abel, R.; Okur, A.; Strockbine, B.; Roitberg, A.; Simmerling, C. Comparison of Multiple Amber Force Fields and Development of Improved Protein Backbone Parameters. *Proteins: Struct., Funct., Bioinf.* **2006**, *65*, 712−725.
(14) Wang, J.; Wolf, R. M.; Caldwell, J. W.; Kollman, P. A.; Case, D. A. Development and Testing of a General Amber Force Field. *J. Comput. Chem.* **2004**, *25*, 1157−1174.
(15) Meagher, K. L.; Redman, L. T.; Carlson, H. A. Development of Polyphosphate Parameters for Use with the AMBER Force Field. *J. Comput. Chem.* **2003**, *24*, 1016−1025.
(16) Allnér, O.; Nilsson, L.; Villa, A. Magnesium Ion-Water Coordination and Exchange in Biomolecular Simulations. *J. Chem. Theory Comput.* **2012**, *8*, 1493−1502.
(17) Baaden, M.; Burgard, M.; Wipff, G. TBP at the Water-Oil Interface: The Effect of TBP Concentration and Water Acidity Investigated by Molecular Dynamics Simulations. *J. Phys. Chem. B* **2001**, *105*, 11131−11141.
(18) Frisch, M. J.; Trucks, G. W.; Schlegel, H. B.; Scuseria, G. E.; Robb, M. A.; Cheeseman, J. R.; Scalmani, G.; Barone, V.; Mennucci, B.; Petersson, G. A.; et al. *Gaussian09*, Revision D.01; Gaussian Inc.: Wallingford, CT, 2009.
(19) Wang, J.; Wang, W.; Kollman, P. A.; Case, D. A. Automatic Atom Type and Bond Type Perception in Molecular Mechanical Calculations. *J. Mol. Graphics Modell.* **2006**, *25*, 247−260.
(20) Case, D.; Babin, V.; Berryman, J.; Betz, R.; Cai, Q.; Cerutti, D.; Cheatham, T., III; Darden, T.; Duke, R.; et al. *AMBER 14*; University of California: San Francisco, 2014.
(21) Jakalian, A.; Jack, D. B.; Bayly, C. I. Fast, Efficient Generation of High-Quality Atomic Charges. AM1-BCC Model: II. Parameterization and Validation. *J. Comput. Chem.* **2002**, *23*, 1623−1641.
(22) Jorgensen, W. L.; Chandrasekhar, J.; Madura, J. D.; Impey, R. W.; Klein, M. L. Comparison of Simple Potential Functions for Simulating Liquid Water. *J. Chem. Phys.* **1983**, *79*, 926−935.
(23) Humphrey, W.; Dalke, A.; Schulten, K. VMD: Visual Molecular Dynamics. *J. Mol. Graphics* **1996**, *14*, 33−38.
(24) Phillips, J.; Braun, R.; Wang, W.; Gumbart, J.; Tajkhorshid, E.; Villa, E.; Chipot, C.; Skeel, R.; Kale, L.; Schulten, K. Scalable Molecular Dynamics With NAMD. *J. Comput. Chem.* **2005**, *26*, 1781−1802.
(25) Andersen, H. C. Rattle: A "Velocity" Version of the Shake Algorithm for Molecular Dynamics Calculations. *J. Comput. Phys.* **1983**, *52*, 24−34.
(26) Darden, T.; York, D.; Pedersen, L. Particle Mesh Ewald: An Nlog(N) Method for Ewald Sums in Large Systems. *J. Chem. Phys.* **1993**, *98*, 10089−10092.
(27) Essmann, U.; Perera, L.; Berkowitz, M. L.; Darden, T.; Lee, H.; Pedersen, L. G. A Smooth Particle Mesh Ewald Method. *J. Chem. Phys.* **1995**, *103*, 8577−8593.
(28) Salomon-Ferrer, R.; Götz, A. W.; Poole, D.; Grand, S. L.; Walker, R. C. Routine Microsecond Molecular Dynamics Simulations with AMBER on GPUs. 2. Explicit Solvent Particle Mesh Ewald. *J. Chem. Theory Comput.* **2013**, *9*, 3878−3888.
(29) Berendsen, H. J. C.; Postma, J. P. M.; van Gunsteren, W. F.; DiNola, A.; Haak, J. R. Molecular Dynamics with Coupling to an External Bath. *J. Chem. Phys.* **1984**, *81*, 3684−3690.
(30) Ryckaert, J.-P.; Ciccotti, G.; Berendsen, H. J. C. Numerical Integration of the Cartesian Equations of Motion of a System With Constraints: Molecular Dynamics of n-Alkanes. *J. Comput. Phys.* **1977**, *23*, 327−341.
(31) Case, D. A.; Darden, T. A.; Cheatham, T. E.; Simmerling, C. L.; Wang, J.; Duke, R. E.; Luo, R.; Walker, R. C.; Zhang, W.; Merz, K. M.; et al. *AMBER 12*; University of California: San Francisco, 2012.
(32) Ramírez, C. L.; Zeida, A.; Jara, G. E.; Roitberg, A. E.; Martí, M. A. Improving Efficiency in SMD Simulations Through a Hybrid Differential Relaxation Algorithm. *J. Chem. Theory Comput.* **2014**, *10*, 4609−4617.
(33) Romero, J. M.; Martin, M.; Ramirez, C. L.; Dumas, V. G.; Marti, M. A. Efficient Calculation of Enzyme Reaction Free Energy Profiles Using a Hybrid Differential Relaxation Algorithm: Application to Mycobacterial Zinc Hydrolases. *Advances in Protein Chemistry and Structural Biology*, 1st ed.; Elsevier Inc., 2015; Vol. *100*, pp 33−65.
(34) Cui, Q.; Elstner, M.; Kaxiras, E.; Frauenheim, T.; Karplus, M. A QM/MM Implementation of the Self-Consistent Charge Density Functional Tight Binding (SCC−DFTB) Method. *J. Phys. Chem. B* **2001**, *105*, 569−585.
(35) Cai, Z.-L.; Lopez, P.; Reimers, J. R.; Cui, Q.; Elstner, M. Application of the Computationally Efficient Self-Consistent-Charge Density-Functional Tight-Binding Method to Magnesium-Containing Molecules. *J. Phys. Chem. A* **2007**, *111*, 5743−5750.
(36) Yang, Y.; Yu, H.; York, D.; Elstner, M.; Cui, Q. Description of Phosphate Hydrolysis Reactions with the Self-Consistent-Charge Density-Functional-Tight-Binding (SCC−DFTB) Theory. 1. Parameterization. *J. Chem. Theory Comput.* **2008**, *4*, 2067−2084.
(37) de M. Seabra, G.; Walker, R. C.; Elstner, M.; Case, D. A.; Roitberg, A. E. Implementation of the SCC−DFTB Method for

DOI: 10.1021/acs.jpcb.6b02527
J. Phys. Chem. B 2016, 120, 6504−6514

Hybrid QM/MM Simulations Within the Amber Molecular Dynamics Package. *J. Phys. Chem. A* **2007**, *111*, 5655−5664.
(38) Jarzynski, C. Nonequilibrium Equality for Free Energy Differences. *Phys. Rev. Lett.* **1997**, *78*, 2690−2693.
(39) Defelipe, L. A.; Lanzarotti, E.; Gauto, D.; Marti, M. A.; Turjanski, A. G. Protein Topology Determines Cysteine Oxidation Fate: The Case of Sulfenyl Amide Formation Among Protein Families. *PLoS Comput. Biol.* **2015**, *11*, No. e1004051, DOI: 10.1371/journal.pcbi.1004051.
(40) Becke, A. D. Density-Functional Thermochemistry. III. The Role of Exact Exchange. *J. Chem. Phys.* **1993**, *98*, 5648−5652.
(41) Stephens, P. J.; Devlin, F. J.; Chabalowski, C. F.; Frisch, M. J. Ab Initio Calculation of Vibrational Absorption and Circular Dichroism Spectra Using Density Functional Force Fields. *J. Phys. Chem.* **1994**, *98*, 11623−11627.
(42) Zhao, Y.; Truhlar, D. G. The M06 Suite of Density Functionals for Main Group Thermochemistry, Thermochemical Kinetics, Noncovalent Interactions, Excited States, and Transition Elements: Two New Functionals and Systematic Testing of Four M06-class Functionals and 12 Other Function. *Theor. Chem. Acc.* **2008**, *120*, 215−241.
(43) Zhao, Y.; Truhlar, D. G. Density Functionals with Broad Applicability in Chemistry. *Acc. Chem. Res.* **2008**, *41*, 157−167.
(44) Heimdal, J.; Kaukonen, M.; Srnec, M.; Rulíšek, L.; Ryde, U. Reduction Potentials and Acidity Constants of Mn Superoxide Dismutase Calculated by QM/MM Free-Energy Methods. *ChemPhysChem* **2011**, *12*, 3337−3347.
(45) Götz, A. W.; Clark, M. A.; Walker, R. C. An Extensible Interface for QM/MM Molecular Dynamics Simulations With AMBER. *J. Comput. Chem.* **2014**, *35*, 95−108.
(46) Hou, G.; Cui, Q. Stabilization of Different Types of Transition States in a Single Enzyme Active Site: QM/MM Analysis of Enzymes in the Alkaline Phosphatase Superfamily. *J. Am. Chem. Soc.* **2013**, *135*, 10457−10469.
(47) Cave-Ayland, C.; Skylaris, C.-K.; Essex, J. W. Direct Validation of the Single Step Classical to Quantum Free Energy Perturbation. *J. Phys. Chem. B* **2015**, *119*, 1017−1025.
(48) Štrajbl, M.; Hong, G.; Warshel, A. Ab Initio QM/MM Simulation with Proper Sampling: "First Principle" Calculations of the Free Energy of the Autodissociation of Water in Aqueous Solution. *J. Phys. Chem. B* **2002**, *106*, 13333−13343.
(49) Hou, G.; Cui, Q. QM/MM Analysis Suggests that Alkaline Phosphatase (AP) and Nucleotide Pyrophosphatase/Phosphodiesterase Slightly Tighten the Transition State for Phosphate Diester Hydrolysis Relative to Solution: Implication for Catalytic Promiscuity In the AP Superfamily. *J. Am. Chem. Soc.* **2012**, *134*, 229−246.
(50) Polyak, I.; Benighaus, T.; Boulanger, E.; Thiel, W. Quantum Mechanics/Molecular Mechanics Dual Hamiltonian Free Energy Perturbation. *J. Chem. Phys.* **2013**, *139*, No. 064105, DOI: 10.1063/1.4817402.
(51) Rod, T. H.; Ryde, U. Quantum Mechanical Free Energy Barrier for an Enzymatic Reaction. *Phys. Rev. Lett.* **2005**, *94*, 138302.
(52) Hudson, P. S.; Woodcock, H. L.; Boresch, S. Use of Nonequilibrium Work Methods to Compute Free Energy Differences Between Molecular Mechanical and Quantum Mechanical Representations of Molecular Systems. *J. Phys. Chem. Lett.* **2015**, *6*, 4850−4856.
(53) Dessauer, C. W.; Gilman, A. G. The Catalytic Mechanism of Mammalian Adenylyl Cyclase. Equilibrium Binding and Kinetic Analysis of P-site Inhibition. *J. Biol. Chem.* **1997**, *272*, 27787−27795.
(54) Göttle, M.; Dove, S.; Kees, F.; Schlossmann, J.; Geduhn, J.; König, B.; Shen, Y.; Tang, W. J.; Kaever, V.; Seifert, R. Cytidylyl and Uridylyl Cyclase Activity of Bacillus Anthracis Edema Factor and Bordetella Pertussis CyaA. *Biochemistry* **2010**, *49*, 5494−5503.
(55) Zwanzig, R. W. High-Temperature Equation of State by a Perturbation Method. I. Nonpolar Gases. *J. Chem. Phys.* **1954**, *22*, 1420−1426.
(56) De Vivo, M.; Dal Peraro, M.; Klein, M. L. Phosphodiester Cleavage in Ribonuclease H Occurs via an Associative Two-Metal-Aided Catalytic Mechanism. *J. Am. Chem. Soc.* **2008**, *130*, 10955−10962.
(57) Palermo, G.; Cavalli, A.; Klein, M. L.; Alfonso-Prieto, M.; Dal Peraro, M.; De Vivo, M. Catalytic Metal Ions and Enzymatic Processing of DNA and RNA. *Acc. Chem. Res.* **2015**, *48*, 220−228.
(58) Palermo, G.; Stenta, M.; Cavalli, A.; Dal Peraro, M.; De Vivo, M. Molecular Simulations Highlight the Role of Metals in Catalysis and Inhibition of Type II Topoisomerase. *J. Chem. Theory Comput.* **2013**, *9*, 857−862.
(59) Kamerlin, S. C. L.; Sharma, P. K.; Prasad, R. B.; Warshel, A. Why Nature Really Chose Phosphate. *Q. Rev. Biophys.* **2013**, *46*, 1−132.
(60) Mildvan, A. Mechanisms of Signaling and Related Enzymes. *Proteins: Struct., Funct., Bioinf.* **1997**, *29*, 401−416.
(61) Hurley, J. H. Structure, Mechanism, and Regulation of Mammalian Adenylyl Cyclase. *J. Biol. Chem.* **1999**, *274*, 7599−7602.
(62) Linder, J. U.; Schultz, J. E. The Class III Adenylyl Cyclases: Multi-Purpose Signalling Modules. *Cell. Signalling* **2003**, *15*, 1081−1089.

DOI: 10.1021/acs.jpcb.6b02527
J. Phys. Chem. B 2016, 120, 6504−6514